Stacked Intelligent Metasurfaces-Aided eVTOL Delay Sensitive Communications

Liyuan Chen, Kai Xiong, *Member, IEEE*, Yujie Qin, *Member, IEEE*, Hanqing Yu, *Member, IEEE*, Supeng Leng, *Member, IEEE*, Chau Yuen, *Fellow, IEEE*

arXiv:2507.06632v1 [cs.NI] 9 Jul 2025

***Abstract*—With rapid urbanization and increasing population density, urban traffic congestion has become a critical issue, and traditional ground transportation methods are no longer sufficient to address it effectively. To tackle this challenge, the concept of Advanced Air Mobility (AAM) has emerged, aiming to utilize low-altitude airspace to establish a three-dimensional transportation system. Among various components of the AAM system, electric vertical take-off and landing (eVTOL) aircraft plays a pivotal role due to their flexibility and efficiency. However, the immaturity of Ultra Reliable Low Latency Communication (URLLC) technologies poses significant challenges to safety-critical AAM operations. Specifically, existing Stacked Intelligent Metasurfaces (SIM)-based eVTOL systems lack rigorous mathematical frameworks to quantify probabilistic delay bounds under dynamic air traffic patterns, a prerequisite for collision avoidance and airspace management. To bridge this gap, we employ network calculus tools to derive the probabilistic upper bound on communication delay in the AAM system for the first time. Furthermore, we formulate a complex non-convex optimization problem that jointly minimizes the probabilistic delay bound and the propagation delay. To solve this problem efficiently, we propose a solution based on the Block Coordinate Descent (BCD) algorithm and Semidefinite Relaxation (SDR) method. In addition, we conduct a comprehensive analysis of how various factors impact regret and transmission rate, and explore the influence of varying load intensity and total delay on the probabilistic delay bound. Under identical meta-atom settings, simulation results indicate that the proposed method achieves a 51.47% average improvement in transmission rate over the low-complexity Alternating Optimization (AO) algorithm. This work provides a theoretical foundation and technical reference for future delay performance optimization and safety assurance in AAM systems.**

***Index Terms*—Advanced air mobility, stacked intelligent metasurfaces, network calculus, semidefinite relaxation method.**

I. Introduction

RECENTLY, rapid urban population growth coupled with escalating transportation demands have exacerbated ground traffic congestion. Conventional transportation infrastructures face significant challenges in accommodating the dynamic mobility requirements of contemporary urban environments, simultaneously contributing to prolonged commute durations and heightened environmental degradation. In response, Advanced Air Mobility (AAM) has emerged as a transformative paradigm that exploits low-altitude airspace to deliver diverse transportation services, encompassing cargo logistics, passenger transit, and emergency response operations [1]. Industry forecasts project the commercial deployment of AAM technologies by 2028, with anticipated annual passenger throughput reaching approximately 440 million by 2050 [2].

Typically, the realization of AAM relies on a suite of advanced technologies, including Unmanned Aerial Vehicles (UAVs) [3], [4], Electric Vertical Take-Off and Landing (eVTOL) aircraft [5], [6], and advanced air traffic management systems [7]. These technologies collectively facilitate a novel transportation paradigm that complements existing ground-based systems. By leveraging the underutilized low-altitude airspace beneath conventional aviation corridors, AAM not only alleviates ground traffic congestion and reduces travel times but also contributes to mitigating the environmental footprint associated with traditional transportation modalities.

Similarly to ground Vehicle-to-Vehicle (V2V) communication systems, eVTOL aircraft necessitate a dedicated aerial communication framework, termed eVTOL-to-eVTOL (eV2V) communication [8], to support cooperative perception and navigation. This communication system is engineered to satisfy the stringent requirements of inter-eVTOL data exchange, networking, and onboard computational capabilities. By facilitating real-time sharing of critical flight parameters among eVTOLs, the system effectively mitigates the risk of mid-air collisions. Consequently, the deployment of eV2V communication enhances airspace utilization efficiency while ensuring the operational safety of AAM networks.

Despite its potential, eV2V communication in AAM systems confronts substantial challenges. In 6G-enabled AAM networks, achieving ultra-low latency, on the order of 1 ms, is essential to guarantee timely and safe operations [9]. Considering the high mobility of low-altitude aerial vehicles, even marginal communication delays can lead to slower response times and elevate the risk of accidents. Consequently, the development of eV2V communication technologies that offer both low latency and high reliability [10], [11] is critical to the safe and efficient functioning of AAM systems.

Compared to conventional Multiple Input Multiple Output (MIMO) antenna systems, Holographic MIMO (HMIMO) systems exhibit enhanced performance in terms of both energy efficiency and transmission capacity [12], [13], [14]. From a hardware perspective, holographic MIMO surfaces (HMIMOS) feature a thinner profile and reduced power consump-

L. Chen, K. Xiong, Y. Qin, H. Yu, and S. Leng are with School of Information and Communication Engineering, University of Electronic Science and Technology of China, Chengdu, 611731, China; and, Shenzhen Institute for Advanced Study, University of Electronic Science and Technology of China, Shenzhen, 518110, China.

C. Yuen is with School of Electrical and Electronics Engineering, Nanyang Technological University, 639798, Singapore.

The corresponding author is Kai Xiong, email: xiongkai@uestc.edu.cn

tion. HMIMO systems combine the multi-antenna benefits of traditional MIMO with advanced signal processing techniques, enabling significantly higher data transmission rates while lowering energy usage [15], thereby contributing to reduced communication latency. By employing HMIMO communication, eVTOL aircraft can sustain high-rate data transmission with decreased battery drain, ultimately extending flight range and enhancing overall endurance.

Conventional HMIMO systems are generally composed of a single-layer metasurface and can be classified into two categories: active HMIMO systems, exemplified by Large Intelligent Surfaces (LIS) [16], and passive HMIMO systems, represented by Reconfigurable Intelligent Surfaces (RIS) [17], [18]. Nevertheless, these architectures are inherently limited in their degrees of freedom for optimization, which restricts their adaptability and performance in dynamic environments.

To overcome these limitations, the concept of Stacked Intelligent Metasurfaces (SIM) has been proposed [19], [20]. By employing a multilayer stacked metasurface architecture, SIM significantly enlarges the optimization space, improves transmission efficiency, and enables signal processing directly in the analog domain. However, investigations into the delay performance of SIM in low-altitude scenarios remain limited, posing challenges to its practical implementation in AAM systems. A primary challenge lies in guaranteeing high reliability while effectively controlling the maximum propagation delay.

This paper presents a systematic analysis of the delay performance of SIM in low-altitude scenarios by leveraging network calculus, a rigorous mathematical framework for performance evaluation. The objective is to provide theoretical insights to support the deployment of SIM within AAM systems. Unlike deterministic network calculus, which only accounts for fixed upper bounds on delay [21], stochastic network calculus enables the characterization of probabilistic delay bounds [22], [23], making it more suitable for complex multi-hop networks with dynamic variations [24]. This approach is particularly critical for collaborative eVTOL scenarios with stringent real-time requirements, as it not only guarantees reliable performance but also facilitates the effective analysis of communication systems subject to high uncertainty and dynamic behaviors.

Based on the aforementioned performance analysis, this paper proposes a framework leveraging the Block Coordinate Descent (BCD) algorithm [25] to decompose the complex optimization problem. To optimize the configuration of SIM phase shifts, a Semidefinite Relaxation (SDR) based strategy [26] is employed, aiming to jointly maximize the transmission rate and minimize the probabilistic delay bound in SIM-enabled communication systems. The main contributions of this paper are summarized as follows:

- We propose a network calculus method-based to SIM-based delay performance analysis for the first time, providing a novel perspective for optimizing low-altitude communication propagation delay by rigorously analyzing the probabilistic upper bound. This study not only addresses a theoretical gap in the delay performance analysis of SIM communication systems but also develops an optimization framework that balances the maximization of transmission rate and the minimization of propagation delay, thereby improving the overall system efficiency and reliability. The proposed framework offers an innovative approach for deploying SIM technology in low-altitude environments, further enhancing its practical value and significance within intelligent low-altitude networks.
- We develope an SDR-based approach to solve the optimization problem, leveraging it to enhance channel gain through precise optimization of the SIM phase shifts, thereby effectively improving the transmission rate. By optimizing the configuration of SIM phase shifts, the SDR method not only reduces propagation delay but also increases the transmission rate, offering an effective solution to improve the overall performance of low-altitude communication systems. This approach establishes a solid foundation for efficient, low-latency communications, and facilitates the advancement of SIM technology in practical deployments.
- Simulation results demonstrate that the proposed BCD algorithm outperforms the low-complexity Alternating Optimization (AO) algorithm in optimizing the transmission rate. Furthermore, we systematically analyze the impact of various parameters on transmission rate and system regret, and investigate the influence of system load and total delay on the probabilistic delay bound.

The remainder of this paper is organized as follows. Section II reviews the related literature. Section III describes the system model. In Section IV, we derive the end-to-end probabilistic delay bound based on stochastic network calculus theory. Section V defines the transmission rate. Section VI formulates the optimization problem and introduces a BCD-based solution method. Section VII presents the simulation results, and Section VIII concludes the paper.

II. Related Work

This section reviews the relevant literature, which can be broadly categorized into three key areas: (i) eVTOL transportation systems, (ii) the fundamentals of stacked intelligent metasurfaces, and (iii) the basic principles of network calculus. A brief overview of related studies in each of these categories is presented below.

A. eVTOL Transportation System

The ongoing acceleration of global urbanization has led to a continuous increase in passenger transportation demand, resulting in intensified traffic congestion on the ground due to overwhelming traffic volume. There is an urgent need for efficient solutions to overcome the limitations of the ground transportation system. One of the most promising approaches is the development of an aerial transportation system based on eVTOL aircraft. eVTOL-based transportation systems are designed to offer a safe, efficient and accessible mode of travel within large urban agglomerations [27].

A typical eVTOL system consists of three core components: the vehicle platform (eVTOL aircraft), the airspace infrastructure (designated air corridors), and the support system (high-reliability communication network). The service scenarios for

the eVTOL systems include primarily: air taxis, air metro, last-mile delivery services, passenger transportation, and emergency service [28], [29].

B. Stacked Intelligent Metasurfaces

In wireless communication systems, traditional RIS generally adopts a single layer metasurface architecture. This design presents significant limitations in beamforming degree of freedom [30] and multi-user interference suppression [20]. To overcome this technical bottleneck, SIM achieves performance leap through an innovative multi-layer stacked metasurfaces structure [19].

A typical SIM system consists of several metasurface layers, with each layer containing multiple meta-atoms. These layers are independently controlled by a Field Programmable Gate Array (FPGA) controller. This hierarchical structure provides SIM with multi-dimensional degree of freedom, enabling layer-by-layer dynamic optimization of electromagnetic parameters such as phase shifts and amplitude. As a result, SIM can precisely reconstruct the spatial electromagnetic field, including the direction of wave propagation, reflection coefficients, polarization characteristics and so on.

Current research demonstrates that SIM technology exhibits significant advantages in various areas, including beamforming [31], SISO/MISO system enhancement [30], channel estimation optimization [32], satellite communication [33], eVTOL communication [34], Direction-of-Arrival (DOA) estimation [35]. However, its application in AAM remains unexplored. In particular, for communication scenarios between eVTOLs, as illustrated in Fig. 1, there is a noticeable gap in the published research on the performance optimization of the SIM-based eV2V communication system. This technological gap needs to be addressed urgently.

C. Stochastic Network Calculus

Stochastic Network Calculus (SNC) is capable of handling stochastic traffic variations in network and utilizes probabilistic tools to provide performance bound [22]. These capability makes network calculus highly applicable in various domains, including optimization of communication network performance [36], Industrial Internet of Things (IIoT) [37], and low-altitude communication network [38].

The following introduces some common concepts in network calculus. Define F as a non-negative, non-decreasing function, and define F^c as a non-negative, non-increasing function. For any random variable X, its distribution function is defined as: $F_X(x) = P(X \leq x)$ The complementary distribution function is defined as: $\bar{F}_X(x) = P(X > x)$. If both X and Y are random variables, for all $x \geq 0$, if $P(X > x) \leq f(x)$, $P(Y > x) \leq g(x)$ then we have [39]: $P(X + Y > x) \leq f(x) \otimes g(x)$, where $\otimes$ denotes the min-plus convolution, which is defined as follows: $f \otimes g(t) = \inf_{0<\tau\leq t}\{f(\tau) + g(t-\tau)\}$.

Let $A(t)$ denotes the arrival process, which represents the cumulative number of bits that have arrived during the time interval $[0, t]$. Similarly, let $S(t)$ denotes the service process, defined as the cumulative number of bits that have been served in the interval $[0, t]$. The departure process, denoted by $A^*(t)$, refers to the cumulative number of bits that have departed within the same interval. For any $0 \leq \tau \leq t$, the arrivals, services and departures in the subinterval $[\tau, t]$ are given by: $A(\tau, t) = A(t) - A(\tau)$, $S(\tau, t) = S(t) - S(\tau)$, $A^*(\tau, t) = A^*(t) - A^*(\tau)$.

For stochastic network calculus [39], a data flow is said to conform to a stochastic arrival curve $\alpha \in F$ with a bounding function $f \in F^c$, denoted as $A \sim \langle f, \alpha \rangle$, if for all $t \geq 0$ and $x \geq 0$, the following inequality holds:

$$P\left\{\sup_{0\leq\tau\leq t}[A(\tau, t) - \alpha(t-\tau)] > x\right\} \leq f(x). \tag{1}$$

Similarly, a server is said to provide a stochastic service curve $\beta \in F$ with a bounding function $g \in F^c$, denoted as $S \sim \langle g, \beta \rangle$, if for all $0 \leq s \leq t$ and $x \geq 0$, it satisfies: $P\{A \otimes \beta(t) - A^*(t) > x\} \leq g(x)$. For a FIFO (First In First Out) system, the delay D at time $t \geq 0$ is given by: $D = \inf\{\tau \geq 0 \mid A(t) \leq A^*(t+\tau)\}$.

III. System Model

In low-altitude intelligent network scenarios, SIM technology offers significant advantages, including a lightweight structure and ease of integration, enabling seamless incorporation into eVTOL aircraft. We consider a bidirectional air-to-air (A2A) communication scenario where two eVTOLs, denoted as eVTOL_A and eVTOL_B, are each equipped with both a transmitter SIM (TX-SIM) and a receiver SIM (RX-SIM), as illustrated in Fig. 1. This configuration enables direct A2A communication between the two aircraft via their respective SIM modules. Through the SIM-enabled A2A communication link, critical real-time information, including flight status, position, altitude, and velocity, can be exchanged to support safe and efficient aerial operations.

Fig. 1: *Illustration of the SIM-Aided A2A Communication between eVTOLs.*

Considering data freshness as a key requirement for flight safety, the communication delay during data packet transmission must be constrained within a reasonable range to avoid potential collision risks. Therefore, in this work, we aim to derive a probabilistic delay bound, $P\{D > T\}$, defined as the probability that the packet delay D exceeds a given threshold T, based on the Stochastic Network Calculus theory.

In the considered system, we make the following red three assumptions: (i) prior to transmission, data packets are temporarily stored in a buffer equipped on eVTOL_A, which

operates under a FIFO principle; (ii) the buffer has sufficient capacity, and issues such as packet loss or retransmission are beyond the scope of this work; and (iii) the service rate is greater than the data arrival rate, ensuring that the queue length remains bounded.

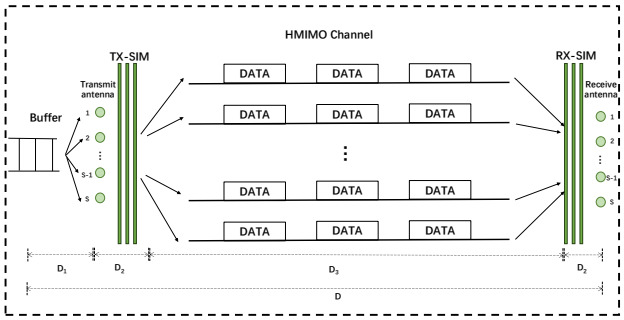

Fig. 2: *Illustration of the End-to-End Packet Delivery Mechanism for eV2V Communication.*

As illustrated in Fig. 2, the total packet delay D consists of the queuing time in the buffer, delays in both the TX- and RX-SIM modules, and the propagation delay over the HMIMO channel. Specifically,

- D_1: **Queuing delay**, denoting the time that data packets wait in the buffer before transmission.
- D_2: **Transmission delay**, accounting for the transmission time from the s-th source to the first metasurface layer of the TX-SIM, as well as the internal transmission delay within the RX-SIM. This delay is considered constant in this work.
- D_3: **Propagation delay**, representing the time required for data packets to be transmitted across the HMIMO channel from the output metasurface of the TX-SIM to the input metasurface of the RX-SIM.

Based on the aforementioned assumptions and system model, we characterize the statistical properties of the total end-to-end delay, D, which can be expressed as the sum of the queuing delay, transmission delay, and propagation delay, $D = D_1 + D_2 + D_3$, and our goal is to derive the probabilistic upper bound on the end-to-end delay, as well as to minimize both the violation probability and the overall delay. These are defined and derived in the following subsections.

Definition 1 (End-to-end Delay of Packets)**.** *The probabilistic upper bound on the end-to-end delay is given by*

$$\bar{D} = P\{D_1 + D_2 + D_3 > T\}, \tag{2}$$

where T denotes the delay threshold. Our objective is to minimize both $\bar{D}$ and T.

IV. SNC-assisted Probabilistic Delay Bound Analysis

In this section, we analyze the upper bound of the total end-to-end delay in the proposed system. We begin by examining the queuing delay in the buffer, which is expressed as a function of the queuing delay. Subsequently, we analyze the propagation delay itself and formulate an optimization problem to minimize it. This, in turn, corresponds to minimize the upper bound of the total packet delay in the considered system.

A. Queueing Delay

In this subsection, we analyze the queuing delay of the data in the buffer. Note that only the queuing delay on the TX-SIM side is considered in this analysis. The upper bound of D_1 is given in the following lemma.

Lemma 1 (Upper Probabilistic Bound of Queueing Delay)**.** *The queueing upper probabilistic bound is given by*

$$\bar{D}_1 = \epsilon(v_{data} B t_b), \tag{3}$$

where $\beta_{data}(t_b)$ is the service curve, t_b is the expected queuing delay, and $\epsilon(\cdot)$ is the bounding function, in case of Poisson arrival process $\epsilon(x) = e^{-\mu x}$, and $\mu > 0$ is a parameter that minimizes the bounding function $\epsilon(x)$, and

$$\beta_{data}(t) = v_{data} B t, \tag{4}$$

in which B denotes the system bandwidth and v_{data} is the transmission rate in the HMIMO channel.

Proof. See Appendix A. □

Recall that we assume the arrival process $A(t)$ follows a Poisson distribution, and the packet size follows an exponential distribution with mean l_d. Let $\delta_d(t)$ denote the number of packets arriving at the HMIMO channel at time t, and let $\delta(t)$ denote the number of packets generated from S sources. In a stable network, we have $\delta_d(t) = \delta(t - D_2)$.

The stochastic arrival curve can then be expressed as [40]:

$$\alpha(t) = \frac{1}{\mu} \log \mathbb{E}[e^{\mu A(t)}] = \frac{\delta_d l_d t}{1 - \mu l_d}, \tag{5}$$

and consequently, according to the stability condition $\alpha(t) \leq \beta(t)$, the optimal value of μ is given by:

$$\mu = \frac{v_{\text{data}} B - \delta_d l_d}{v_{\text{data}} B l_d}. \tag{6}$$

Lemma 2 (Queueing Probabilistic Delay Bound in Case of Poisson Arrival Process)**.** *Combining the bounding function $\epsilon(x) = e^{-\mu x}$ and* (6)*, the probabilistic delay bound of D_1 in case of Poisson arrival process is given by:*

$$\bar{D}_1(t_b) = e^{-\mu v_{data} B t_b} = e^{-\frac{v_{data} B - \delta_d l_d}{l_d} t_b}. \tag{7}$$

B. Transmission delay

Assume that there are S data streams in total. The TX-SIM consists of L metasurface layers, each containing M meta-atoms, where $M \geq S$. Similarly, the RX-SIM is composed of K metasurface layers, each with N meta-atoms, and $N \geq S$. Under these conditions, the transmission delay D_2 can be expressed as

$$D_2 = \max\left(\frac{d_{s,\text{TX}} + d_{A-\text{TX}}}{v_{\text{TX}}} + \frac{d_{B-\text{RX}} + d_{\text{RX},s}}{v_{\text{RX}}}\right), \tag{8}$$

where v_{TX} and v_{RX} denote the electromagnetic wave propagation speeds within the TX-SIM and RX-SIM, respectively.

The term $d_{s,\mathrm{TX}}$ represents the distance between the s-th data source and the m-th meta-atom in the input metasurface layer of the TX-SIM, while $d_{\mathrm{RX},s}$ denotes the distance between the n-th meta-atom in the output metasurface layer of the RX-SIM and the s-th data source. The total intra-device propagation distances within the TX-SIM and RX-SIM are denoted by $d_{A\text{-}TX}$ and $d_{B\text{-}RX}$, respectively. The values of $d_{s,\mathrm{TX}}$ and $d_{\mathrm{RX},s}$ can be calculated using the following formula

$$a_{TX} = \left(m_z - \frac{m^r_{\max}+1}{2}\right) r_{\mathrm{tx}} - \left(s - \frac{S+1}{2}\right)\frac{\lambda}{2}, \quad (9)$$

$$a_{RX} = \left(n_z - \frac{n^r_{max}+1}{2}\right) r_{rx} - \left(s - \frac{S+1}{2}\right)\frac{\lambda}{2}, \quad (10)$$

$$b_{TX} = m_x - \frac{m^r_{max}+1}{2} r_{tx},\ b_{RX} = n_x - \frac{n^r_{max}+1}{2} r_{rx}, \quad (11)$$

$$d_{s,\mathrm{TX}} = \sqrt{a^2_{TX} + b^2_{TX} + d^2_t},\ d_{\mathrm{RX},s} = \sqrt{a^2_{RX} + b^2_{RX} + d^2_r}, \quad (12)$$

where $m_z = \lceil \frac{m}{m^r_{\max}} \rceil$ and $n_z = \lceil \frac{n}{n^r_{\max}} \rceil$ represent the z-axis indices of the m-th and n-th meta-atoms in the TX-SIM and RX-SIM, respectively. Similarly, let $m_x = \mathrm{mod}(m-1, m^r_{\max})+1$ and $n_x = \mathrm{mod}(n-1, n^r_{\max})+1$ represent their respective x-axis indices, $m^r_{\max}$ denotes the maximum number of meta-atoms per row on each metasurface layer of the TX-SIM, while $n^r_{\max}$ denotes the same for the RX-SIM. The parameters r_{tx} and r_{rx} represent the distances between adjacent meta-atoms on each metasurface layer of the TX-SIM and RX-SIM, respectively. Let λ denote the signal wavelength. The vertical spacing between metasurface layers in the TX-SIM is given by $d_t = \frac{D_t}{L}$, where D_t is the total thickness of the TX-SIM and L is the number of metasurface layers. Similarly, $d_r = \frac{D_r}{K}$ denotes the vertical spacing between metasurface layers in the RX-SIM, where D_r is the total thickness and K is the number of layers.

Next, we calculate $d_{\text{A-TX}}$ and $d_{\text{B-RX}}$, where $d_{\text{A-TX}}$ denotes the transmission distance of the s-th data stream within the TX-SIM of $eVTOL_A$, and $d_{\text{B-RX}}$ denotes the transmission distance of the s-th data stream within the RX-SIM of $eVTOL_B$. The corresponding formulas are given as follows

$$d_{A-RX} = \sum_{l=2}^{\mathrm{L}} d^{\mathrm{l}}_{A-RX},\ d_{B-RX} = \sum_{k=2}^{\mathrm{K}} d^{\mathrm{k}}_{B-RX}, \quad (13)$$

$$\mathrm{d}^{\mathrm{l}}_{\mathrm{A-TX}} = \sqrt{\mathrm{r}^{l}_{\mathrm{m_A},\ \mathrm{m'_A}}{}^2 + \mathrm{d}^2_{\mathrm{t}}} \quad l \in [2, L], \quad (14)$$

$$d^{\mathrm{k}}_{B-RX} = \sqrt{\mathrm{r}^{k}_{\mathrm{n_B},\ \mathrm{n'_B}}{}^2 + \mathrm{d}^2_{\mathrm{r}}} \quad k \in [2, K], \quad (15)$$

where $d^l_{\text{A-TX}}$ denotes the distance between the m_A-th meta-atom on the $(l-1)$-th layer and the m'_A-th meta-atom on the l-th layer of the TX-SIM in $eVTOL_A$. Similarly, $d^k_{B\text{-RX}}$ represents the distance between the n_B-th meta-atom on the $(k-1)$-th layer and the n'_B-th meta-atom on the k-th layer of the RX-SIM in $eVTOL_B$. The term $\mathrm{r}^1_{m_A,m'_A}$ denotes the horizontal spacing between the m_A-th and m'_A-th meta-atoms on the same metasurface layer of $eVTOL_A$. Likewise, $\mathrm{r}^k_{n_B,n'_B}$ denotes the spacing between the n_B-th and n'_B-th meta-atoms on the same metasurface layer of $eVTOL_B$. The expressions for $\mathrm{r}^1_{m_A,m'_A}$ and $\mathrm{r}^k_{n_B,n'_B}$ are given as follows:

$$\mathrm{r}^1_{\mathrm{m_A},\ \mathrm{m_A'}} = \mathrm{r_{tx}}\sqrt{(\ \mathrm{m_z} - \mathrm{m'_z})^2 + (\mathrm{m_x} - \mathrm{m'_x})^2}, \quad (16)$$

$$\mathrm{r}^k_{\mathrm{n_B},\ \mathrm{n_B'}} = \mathrm{r_{rx}}\sqrt{(\ \mathrm{n_z} - \mathrm{n'_z})^2 + (\mathrm{n_x} - \mathrm{n'_x})^2}. \quad (17)$$

Finally, we are ready to derive the upper bound which is a fixed constant of the transmission delay, as given in the following lemma.

Lemma 3 (Upper Bound of Transmission Delay)**.** *The upper bound of the transmission delay is given by:*

$$D_2 = \max\Big(\frac{\sqrt{a^2_{TX} + b^2_{TX} + d^2_t} + \sum_{l=2}^{L}\sqrt{r^1_{m_A,m'_A} + d^2_t}}{v_{TX}} + \frac{\sqrt{a^2_{RX} + b^2_{RX} + d^2_r} + \sum_{k=2}^{K}\sqrt{r^2_{n_B,n'_B} + d^2_r}}{v_{RX}}\Big). \quad (18)$$

Proof. The result in (18) is obtained by combining (8)–(17). □

C. Propagation Delay

The upper probabilistic bound of the propagation delay $\bar{D}_3(t)$ for transmitting S packets in the HMIMO channel can be expressed in the following lemma.

Lemma 4 (Upper Probabilistic Bound of Propagation Delay)**.** *The upper probabilistic bound of propagation delay is given by:*

$$P\{D_3 > t_d\} \le \bar{D}_3(t_d). \quad (19)$$

Proof. The upper bound of D_3 is computed as follows:

$$P\{D_3 > t_d\} = P\left\{\frac{Sl_d}{v_{\mathrm{data}}B} > t_d\right\} = P\left\{l_d > \frac{v_{\mathrm{data}}Bt_d}{S}\right\}. \quad (20)$$

Let $f_L(l)$ be the probability density function (PDF) of l_d, the bounding function of t_d is

$$\bar{D}_3(t_d) = \int_{\frac{v_{\mathrm{data}}Bt_d}{S}}^{\infty} f_L(l)\, dl = e^{-\frac{v_{\mathrm{data}}B}{Sl_d}t_d}. \quad (21)$$

□

Now that the upper probabilistic bounds of D_1 and D_3 have been derived, we proceed to present the total upper probabilistic bound of the end-to-end delay in the following theorem. To facilitate the derivation, we first introduce a prerequisite lemma.

Lemma 5. *Let $Z = \sum_{i=1}^{N} X_i$, where Z and X_i are random variables. Then, the complementary cumulative distribution function (CCDF) of Z satisfies the following inequality*

$$\bar{F}_Z(x) \le \bar{F}_{X_1} \otimes \bar{F}_{X_2} \otimes \cdots \otimes \bar{F}_{X_N}(x), \quad (22)$$

where $\bar{F}_Z(x)$ denotes the CCDF of Z with respect to the variable x, and $\otimes$ represents the min-plus convolution operator.

Based on Lemma 5 and the statistical properties of D_1, D_2, and D_3, we now establish the upper probabilistic bound of the total end-to-end delay as follows.

Theorem 1 (Upper probabilistic bound of D)**.** *According to Lemma 5, the upper probability bound of the total delay is*

$$\bar{D} = \inf_{\mathrm{t_1+t_3=T-D_2}} \left\{ \mathrm{e}^{-\frac{\mathrm{v}_{data}\mathrm{B}-\delta_\mathrm{d}\mathrm{l_d}}{\mathrm{l_d}}\mathrm{t_b}} + \mathrm{e}^{-\frac{\mathrm{v}_{data}\mathrm{B}}{\mathrm{Sl_d}}\mathrm{t_d}} \right\}. \tag{23}$$

Proof. The upper bound $\bar{D}$ is computed as

$$\begin{aligned} \bar{D} &= P\{\mathrm{D} > \mathrm{t}\} = \mathrm{P}\left\{\mathrm{D_1(t)} + \mathrm{D_3(t)} > \mathrm{T} - \mathrm{D_2}\right\} \\ &\leq \mathrm{f_{D_1}}\left(\mathrm{t_b}\right) \otimes \mathrm{f_{D_3}}\left(\mathrm{t_d}\right), \end{aligned} \tag{24}$$

proof completes by substituting the CCDF of D_1 and D_3, as given in (7) and (21), respectively. □

We now derive the upper probabilistic bound of the delays associated with buffering, radio propagation, and transmission, and express the upper probabilistic bound of the total delay as a function of v_{data} and t_d, which are key parameters related to SIM-assisted transmission. In the following section, we analyze the optimal values of v_{data} and t_d that minimize the total delay T and the total end-to-end probabilistic bound.

V. SIM-based Performance Optimization

Following the derivation of the probabilistic upper bound on the total end-to-end delay $\bar{D}$, a critical aspect remains to be addressed: the determination of the data transmission rate within the HMIMO channel. This transmission rate, denoted by v_{data}, directly influences the propagation delay t_d and serves as a fundamental parameter in the performance evaluation of the proposed communication system. In the subsequent analysis, we derive an analytical expression for v_{data}.

The transmission rate in the HMIMO channel can be characterized to provide a quantitative basis for subsequent delay analysis [41]. Let $\theta_m^l \in [0, 2\pi)$ denote the phase shift of the m-th meta-atom in the l-th metasurface layer of the TX-SIM, where $m \in [1, M]$ and $l \in [1, L]$. The corresponding transmission coefficient is given by $\phi_m^l = e^{j\theta_m^l}$. The phase shift vector of the l-th layer is defined as $\boldsymbol{\phi}^1 = \left[\phi_1^1, \phi_2^1, \ldots, \phi_M^1\right]^{\mathrm{T}} \in \mathbb{C}^{M\times 1}$, and the associated transmission coefficient matrix is expressed as $\boldsymbol{\Phi}^1 = \mathrm{diag}[\Phi^1] \in \mathbb{C}^{M\times M}$. Similarly, let $\xi_n^k \in [0, 2\pi)$ denote the phase shift of the n-th meta-atom in the k-th layer of the RX-SIM, where $n \in [1, N]$ and $k \in [1, K]$. The corresponding transmission coefficient is given by $\psi_n^k = e^{j\xi_n^k}$. The phase shift vector of the k-th layer is defined as $\boldsymbol{\psi}^k = \left[\psi_1^k, \psi_2^k, ..., \psi_N^k\right]^T \in \mathbb{C}^{N\times 1}$ and the corresponding transmission coefficient matrix is $\boldsymbol{\Psi}^1 = \mathrm{diag}[\boldsymbol{\psi}^k] \in \mathbb{C}^{N\times N}$.

According to [19], the transmission coefficient from the m'_A-th meta-atom in the $(l-1)$-th layer to the m_A-th meta-atom in the l-th layer of the TX-SIM carried by $eVTOL_A$ is given by

$$\mathrm{w}^1_{\mathrm{m},\ \mathrm{m'}} = \frac{\mathrm{C_t}\cos\chi^1_{\mathrm{m},\ \mathrm{m'}}}{d^l_{A-TX}}\left(\frac{1}{2\pi d^l_{A-TX}} - \mathrm{j}\frac{1}{\lambda}\right)\mathrm{e}^{\frac{\mathrm{j}2\pi d^l_{A-TX}}{\lambda}}, \tag{25}$$

where $d^l_{A\text{-TX}}$ denotes the distance between the m-th meta-atom in the l-th metasurface layer and the m'-th meta-atom in the $(l-1)$-th layer, with $l \in [2, L]$. Here, C_t is the effective area of each meta-atom in the TX-SIM, and $\chi^l_{m,,m'}$ is the angle between the wave propagation direction from the $(l-1)$-th layer and the normal vector of the l-th metasurface layer.

Let $\mathbf{W}^l \in \mathbb{C}^{M\times M}$ denote the transmission coefficient matrix that characterizes the electromagnetic interaction between the l-th and $(l-1)$-th metasurface layers of the TX-SIM, for $l \in [2, L]$. Specifically, $\mathbf{W}^1 \in \mathbb{C}^{M\times S}$ represents the transmission coefficient matrix mapping the S input data streams to the first metasurface layer. Accordingly, the overall transformation implemented by the TX-SIM can be expressed as:

$$\mathbf{X} = \boldsymbol{\Phi}^L\mathbf{W}^L\boldsymbol{\Phi}^{L-1}\mathbf{W}^{L-1}\ldots\boldsymbol{\Phi}^2\mathbf{W}^2\boldsymbol{\Phi}^1\mathbf{W}^1 \in \mathbb{C}^{M\times S}. \tag{26}$$

Similarly, for the RX-SIM, the transmission coefficient from the n'-th meta-atom in the $(k-1)$-th metasurface layer to the n-th meta-atom in the k-th layer is given by

$$u^k_{n,n'} = \frac{C_r\cos\zeta^k_{n,n'}}{d^k_{\mathrm{B-RX}}}\left(\frac{1}{2\pi d^k_{\mathrm{B-RX}}} - \frac{1}{j\lambda}\right)e^{j2\pi d^k_{B-RX}/\lambda}, \tag{27}$$

where $d^k_{B\text{-RX}}$ denotes the transmission distance between the n'-th meta-atom in the $(k-1)$-th metasurface layer and the n-th meta-atom in the k-th layer. The parameter C_r represents the effective area of each unit meta-atom in the RX-SIM, and $\zeta^k_{n,n'}$ denotes the angle between the propagation direction from the $(k-1)$-th layer and the normal vector of the k-th metasurface layer.

Let $\mathbf{U}^k \in \mathbb{C}^{N\times N}$ denote the transmission coefficient matrix representing the electromagnetic coupling between the $(k-1)$-th and k-th metasurface layers within the RX-SIM, for $k \in [2, K]$. Specifically, $\mathbf{U}^K \in \mathbb{C}^{S\times N}$ denotes the transmission coefficient matrix that maps the output of the final metasurface layer to the S output data streams. Accordingly, the overall transformation induced by the RX-SIM can be expressed as:

$$\mathbf{Y} = \mathbf{U}^K\boldsymbol{\Psi}^K\mathbf{U}^{K-1}\boldsymbol{\Psi}^{K-1}\ldots\mathbf{U}^2\boldsymbol{\Psi}^2\mathbf{U}^1\boldsymbol{\Psi}^1 \in \mathbb{C}^{S\times N}. \tag{28}$$

Consequently, the end-to-end channel matrix in HMIMO channel is given by

$$\mathbf{H} = \mathbf{YGX}, \tag{29}$$

where $\mathbf{G} = \mathbf{R}_{\mathrm{RX}}^{1/2}\bar{\mathbf{G}}\mathbf{R}_{\mathrm{TX}}^{1/2} \in \mathbb{C}^{N\times M}$ is the channel matrix as described in [42], $\bar{\mathbf{G}}$ represents an independent and identically distributed (i.i.d.) Rician fading channel. The matrices $\mathbf{R}_{\mathrm{TX}} \in \mathbb{C}^{M\times M}$ and $\mathbf{R}_{\mathrm{RX}} \in \mathbb{C}^{N\times N}$ denote the spatial correlation matrices at the TX-SIM and RX-SIM, respectively. The explicit forms of these correlation matrices are provided in [43] as:

$$\begin{aligned} \left[\mathbf{R}_{\mathrm{TX}}\right]_{\mathrm{m_A,m_A'}} &= \mathrm{sinc}\left(\frac{2\mathrm{r}^l_{\mathrm{m_A,m_A'}}}{\lambda}\right), \quad \mathrm{m,m'} \in [1, M], \\ \left[\mathbf{R}_{\mathrm{RX}}\right]_{\mathrm{n_B,n_B'}} &= \mathrm{sinc}\left(\frac{2\mathrm{r}^k_{\mathrm{n_B,n_B'}}}{\lambda}\right), \quad \mathrm{n,n'} \in [1, N]. \end{aligned} \tag{30}$$

The channel matrix describing the electromagnetic propagation from the output metasurface layer of the TX-SIM to

the input metasurface layer of the RX-SIM can be expressed as

$$\bar{\mathbf{G}}^{\mathrm{H}} = \sqrt{\gamma}\left(\sqrt{\frac{\kappa}{1+\kappa}}\mathbf{h}_{\mathrm{LoS}}^{\mathrm{H}} + \sqrt{\frac{1}{1+\kappa}}\mathbf{h}_{\mathrm{NLoS}}^{\mathrm{H}}\right) \in \mathbb{C}^{N\times M}, \tag{31}$$

where κ is the Rician factor, $\gamma = 10^{-\frac{PL(d_{eVTOL})}{10}}$ is the channel gain, d_{eVTOL} is the distance between eVTOL$_A$ and eVTOL$_B$. $\mathbf{h}_{\mathbf{LoS}}^{\mathbf{H}} \in \mathbb{C}^{N\times M}$ is the Line-of-Sight (LoS) coefficient and $\mathbf{h}_{\mathbf{NLoS}}^{\mathbf{H}} \in \mathbb{C}^{N\times M}$ is the Non LoS (NLoS) coefficient. $\mathrm{PL}(\mathrm{d_{eVTOL}})$ can be provided by

$$\begin{aligned}\mathrm{PL}(d_{\mathrm{eVTOL_A}}) &= \mathrm{PL}(d_0) + 10\eta\log_{10}\left(\frac{d_{\mathrm{eVTOL}}}{d_0}\right),\\ \mathrm{PL}(d_0) &= 20\log_{10}\left(\frac{4\pi d_0}{\lambda}\right), \quad \lambda = \frac{c}{f},\end{aligned} \tag{32}$$

where η denotes the path loss exponent, $\mathrm{PL}(d_0)$ represents the reference path loss at a distance d_0, and d_0 is the reference distance. The parameter λ is the carrier wavelength, f is the operating frequency, and c is the speed of light in free space, with $c = 3\times 10^8$ m/s.

The received channel vector is modeled as

$$\mathbf{y} = \mathbf{H}\mathbf{x} + \mathbf{n}, \tag{33}$$

where $\mathbf{x} \in \mathbb{C}^{S\times 1}$ denotes the transmitted signal vector, and $\mathbf{n} \in \mathbb{C}^{S\times 1}$ is the additive noise vector, modeled as a circularly symmetric complex Gaussian random vector, i.e., $\mathbf{n} \sim \mathcal{CN}(0, N_0\mathbf{I})$, where N_0 denotes the noise power spectral density, and the matrix $\mathbf{H} \in \mathbb{C}^{S\times S}$ represents the channel matrix.

Suppose the average transmission power is constrained by $\mathbb{E}\{\mathbf{x}^H\mathbf{x}\} \le P$, where P denotes the total transmission power, the achievable transmission data can be derived in the following theorem.

Theorem 2 (Achievable Transmission Data Rate)**.** *Given the HMIMO channel matrix $\mathbf{H} \in \mathbb{C}^{S\times S}$ and the identity matrix $\mathbf{I} \in \mathbb{C}^{S\times S}$, the achievable transmission data rate v_{data} as given in [41] can be expressed as*

$$v_{data} = \log_2\det\left(\mathbf{I} + \frac{\mathbf{HZH}^H}{N_0 B}\right), \tag{34}$$

where $\mathbf{Z} = \mathbb{E}\{\mathbf{x}\mathbf{x}^H\} \in \mathbb{C}^{S\times S}$ is a positive semi-definite matrix denotes the covariance matrix of the transmitted signal $\mathbf{x}$.

VI. Problem Formulation and Optimization

A. Problem Formulation

This section aims to maximize the data transmission rate v_{data} in the HMIMO channel while minimizing the propagation delay t_d, thereby achieving the joint objective of reducing both the probabilistic delay upper bound $\bar{D} = P\{D > T\}$ and the total end-to-end delay, T. Given that the transmission delay, D_2 is fixed, and assuming an expected queuing delay denoted by t_b, the total end-to-end delay can be expressed as:

$$\begin{aligned}\mathcal{P}1: \min_{v_{\mathrm{data}},\, t_d} \quad & f(v_{\mathrm{data}}, t_d) = \mathrm{e}^{-\frac{\mathrm{v_{data}B}-\delta_{\mathrm{d}}\mathrm{l_d}}{\mathrm{l_d}}\mathrm{t_b}} + \mathrm{e}^{-\frac{\mathrm{v_{data}B}}{\mathrm{Sl_d}}\mathrm{t_d}} + t_d\\ \text{s.t.} \quad & \mathrm{t_d} = \mathrm{T} - \mathrm{D_2} - \mathrm{t_b},\\ & \theta_{\mathrm{m}}^1 \in (0, 2\pi],\ \xi_{\mathrm{n}}^{\mathrm{k}} \in (0, 2\pi].\end{aligned} \tag{35}$$

Note that, to simplify the optimization problem, we assume that the transmit power is uniformly allocated among all data streams.

To address the complexity of this non-convex optimization problem, we adopt a hybrid solution strategy. First, the BCD method is employed to decompose the problem, thereby reducing its computational difficulty by alternately optimizing over different subsets of variables. Next, the SDR technique is applied to convert the resulting non-convex subproblems into convex formulations, which can be efficiently solved via Semidefinite Programming (SDP). To recover a feasible solution from the relaxed SDR output, the Gaussian Randomization method is subsequently used for post-processing. This integrated framework—comprising BCD-based iterative optimization, SDR-based convex relaxation, and Gaussian randomization for solution recovery—strikes a balance between computational efficiency and solution quality, and provides a practical approach for solving the original non-convex problem.

B. The Proposed BCD Algorithm

In this work, we introduce the BCD algorithm into the optimization framework. The algorithmic process is illustrated as follows.

Algorithm 1: BCD Algorithm

1 **Input**: Propagation delay t_d, transmission rate in HMIMO channel v_{data}
2 **Output**: Updated data transmission rate v_{data}, updated propagation delay t_d
3 Initialize the propagation delay $t_d \leftarrow 0.6s$
4 **for** $iteration = 1, 2, \cdots, max_iterations$ **do**
5 Fix t_d, calculate the rate in the HMIMO channel, and update the phase shifts of each metasurface layer on SIM by using SDR method;
6 Fix v_{data}, optimize t_d using an optimizer and update the total end-to-end delay T;
7 Calculate the result according to the objective function of f_{v_{data},t_d};
8 **return** *the value of regret, updated propagation delay t_d, upper probabilistic delay bound*

As the first step, by fixing the propagation delay t_d, the original problem $\mathcal{P}1$ is transformed into a simplified subproblem $\mathcal{P}2$, which involves optimization solely with respect to the data transmission rate v_{data}. Although $\mathcal{P}2$ remains a non-convex and computationally challenging problem, it will be addressed in the subsequent subsection VI-C using the Semidefinite Relaxation technique.

$$\begin{aligned}\mathcal{P}2: \min_{\mathrm{v_{data}}} \quad & f\left(\mathrm{v_{data}}, \mathrm{t_d}\right) = \mathrm{e}^{-\frac{\mathrm{v_{data}B}-\delta_{\mathrm{d}}\mathrm{l_d}}{\mathrm{l_d}}\mathrm{t_b}} + \mathrm{e}^{-\frac{\mathrm{v_{data}B}}{\mathrm{Sl_d}}\mathrm{t_d}} + \mathrm{C}_1\\ & \text{s.t. } \theta_{\mathrm{m}}^1 \in (0, 2\pi], \quad \xi_{\mathrm{n}}^{\mathrm{k}} \in (0, 2\pi],\end{aligned} \tag{36}$$

where $C_1 = \rho t_d$ be a predefined constant related to the propagation delay. Assuming that v_{data} has been updated in

the current iteration, we subsequently fix its value to optimize t_d, resulting in the reformulated subproblem denoted as $\mathcal{P}3$.

$$\begin{aligned} \mathcal{P}3: \min_{\mathrm{t_d}} \quad & f\left(\mathrm{t_d}\right)=\mathrm{e}^{-\frac{\mathrm{v_{data}\ B}}{\mathrm{Sl_d}}\mathrm{t_d}}+\rho \mathrm{t_d}+\mathrm{C}_2 \\ & \text{s.t. } \mathrm{t_d}=\mathrm{T}-\mathrm{D}_2-\mathrm{t_b}. \end{aligned} \tag{37}$$

In this case, let $C_2 = e^{-\frac{(v_{\text{data}}B-\delta_d l_d)}{l_d}t_b}$. With this substitution, the subproblem $\mathcal{P}3$ reduces to a basic convex optimization problem. This illustrates the effectiveness of the BCD algorithm in handling this class of structured non-convex problems by decomposing them into tractable subproblems.

$$\begin{aligned} \nabla f\left(t_d\right) &= -\frac{v_{\text{data}}\, B}{Sl_d} e^{-\frac{v_{data}B}{Sl_d}t_d}+\rho, \\ t_d &= -\frac{Sl_d}{v_{\text{data}}\, B}\ln\left(\frac{\rho Sl_d}{v_{\text{data}}\, B}\right). \end{aligned} \tag{38}$$

We directly derive the closed-form solution for the optimal propagation delay t_d. Once the optimal t_d is obtained, the optimal total delay T can be computed by the constraint $T = D_2 + t_b + t_d$, and the probabilistic delay bound $\bar{D}$ can be subsequently evaluated.

C. The Proposed Semidefinite Relaxation Method

After applying the BCD method to decompose the original problem, it follows that minimizing the objective function $f(v_{\text{data}})$, while treating all other variables as constants, is equivalent to maximizing the data transmission rate v_{data} in the HMIMO channel. Accordingly, the original optimization problem $\mathcal{P}2$ can be simplified to the following problem, denoted as $\mathcal{P}4$:

$$\begin{aligned} \mathcal{P}4: \max_{\phi^{\mathrm{l}},\psi^{\mathrm{k}}} \quad & \mathrm{v_{data}}\ =\log_2\det\left(\mathbf{I}+\frac{\mathbf{HZH}^{\mathrm{H}}}{\mathrm{N_0\ B}}\right) \\ \text{s.t.} \quad & \theta_{\mathrm{m}}^{\mathrm{l}}\in(0,2\pi], \qquad \xi_{\mathrm{n}}^{\mathrm{k}}\in(0,2\pi]. \end{aligned} \tag{39}$$

Clearly, to maximize v_{data}, it is essential to maximize the effective channel gain characterized by $\mathbf{HZH}^H$. Given that the channel matrix $\mathbf{H}$ is directly influenced by the phase shifts within the transmission coefficient matrices, the optimization problem can ultimately be reformulated as one targeting the HMIMO channel matrix $\mathbf{H}$. In other words, by judiciously controlling the phase shifts, the transmission rate of the HMIMO channel can be enhanced, which is critical for improving overall system performance. Another definition of $\mathbf{H}$ is provided as follows

$$\begin{aligned} \mathbf{H} &= \mathbf{U}^1\mathbf{\Psi}^1\cdots\mathbf{U}^K\mathbf{\Psi}^K\,\mathbf{G}\,\mathbf{\Phi}^L\mathbf{W}^L\cdots\mathbf{\Phi}^1\mathbf{W}^1 \\ &= \boldsymbol{h}_{\mathrm{SIM},r}^{\mathrm{H}}\,\mathbf{\Omega}\,\boldsymbol{h}_{t,\mathrm{SIM}}, \end{aligned} \tag{40}$$

where $\mathbf{h}_{\text{SIM},r}$ denotes the channel coefficient matrix from the p-th metasurface layer of the SIM to the receiver, with $p \in [1, \max(L, K)]$. The transmission coefficient matrix is defined as $\mathbf{\Omega} = \text{diag}(e^{j\Omega_1}, \ldots, e^{j\Omega_{\mathrm{a}}}) \in \mathbb{C}^{\mathrm{a}\times\mathrm{a}}$, where Ω_{a} represents the phase shifts of the single-layer SIM subject to optimization. Depending on whether the phase shifts of the TX-SIM or RX-SIM are being optimized, we set $\Omega = \boldsymbol{\phi}$ or $\Omega = \boldsymbol{\psi}$, respectively. The parameter a denotes the number of meta-atoms in the metasurface layer, which varies according to whether the transmission coefficient matrix corresponds to the TX-SIM or RX-SIM. Furthermore, $\mathbf{h}_{\text{t,SIM}}$ denotes the channel coefficient matrix from the transmitter to the p-th metasurface layer of the SIM. The channel coefficient matrices under different optimization objectives are expressed as following two scenarios,

(i) if the phase shifts of TX-SIM is being optimized, then we have

$$\begin{aligned} \boldsymbol{h}_{SIM,r} &= \mathbf{Y}\mathbf{G}\mathbf{\Phi}^L\mathbf{W}^L\cdots\mathbf{\Phi}^{p+1}\mathbf{W}^{p+1}, \\ \boldsymbol{h}_{t,SIM} &= \mathbf{W}^p\mathbf{\Phi}^{p-1}\mathbf{W}^{p-1}\cdots\mathbf{\Phi}^1\mathbf{W}^1. \end{aligned} \tag{41}$$

(ii) if the phase shifts of RX-SIM is being optimized, then we have

$$\begin{aligned} \boldsymbol{h}_{SIM,r} &= \mathbf{U}^1\mathbf{\Psi}^1\cdots\mathbf{U}^{p-1}\mathbf{\Psi}^{p-1}\mathbf{U}^p, \\ \boldsymbol{h}_{t,SIM} &= \mathbf{U}^{p+1}\mathbf{\Psi}^{p+1}\cdots\mathbf{U}^K\mathbf{\Psi}^K\mathbf{G}\mathbf{X}. \end{aligned} \tag{42}$$

It is important to note that the phase shift values contained in the matrices $\mathbf{X}$ and $\mathbf{Y}$ are iteratively updated throughout the progression of the BCD algorithm.

Based on the aforementioned channel model, the original optimization problem $\mathcal{P}4$ can be further reformulated as the optimization problem $\mathcal{P}5$

$$\begin{aligned} \mathcal{P}5: \max_{\Omega} & \sum_{s=1}^{S}||\boldsymbol{h}_{SIM,r,s}^H\mathbf{\Omega}\boldsymbol{h}_{t,SIM}||^2 \\ \text{s.t. } & 0\le\Omega_{\mathrm{a}}\ \le 2\pi \quad \mathrm{a}\ \in[1,\max\{M,N\}], \end{aligned} \tag{43}$$

where $\boldsymbol{h}_{\text{SIM},r,s}^H \in \mathbb{C}^{1\times\mathrm{a}}$ denotes the channel coefficient vector from the p-th metasurface layer of the SIM to the receiver for the s-th data flow. The vector $\boldsymbol{v} = [v_1, v_2, \ldots, v_{\mathrm{a}}]^T \in \mathbb{C}^{\mathrm{a}\times 1}$ is defined such that each element $v_{\mathrm{a}} = e^{j\Omega_{\mathrm{a}}}$ corresponds to the phase shift of a meta-atom. The constraint on the phase shifts can be equivalently expressed as a unit-modulus constraint, i.e., $|v_{\mathrm{a}}|^2 = 1$, which leads to the following formulation

$$\sum_{s=1}^{S}||\boldsymbol{h}_{SIM,r,s}^H\mathbf{\Omega}\boldsymbol{h}_{t,SIM}||^2=\sum_{s=1}^{S}||\boldsymbol{v}^H\mathbf{\Lambda}_s||^2, \tag{44}$$

where $\mathbf{\Lambda}s = \text{diag}\left(\boldsymbol{h}_{\text{SIM},r,s}^H\right)$ and $\boldsymbol{h}_{t,\text{SIM}} \in \mathbb{C}^{\mathrm{a}\times S}$, thereby leading to the formulation of problem $\mathcal{P}6$ as shown as:

$$\begin{aligned} \mathcal{P}6: \quad & \max_{\mathbf{v}}\sum_{s=1}^{S}\mathbf{v}^H\mathbf{\Lambda}_s\mathbf{\Lambda}_s^H\mathbf{v} \\ & \text{s.t. } |\mathbf{v}_{\mathrm{a}}|^2=1,\ \mathrm{a}\ \in[1,\max\{M,N\}]. \end{aligned} \tag{45}$$

This transformation results in a Quadratically Constrained Quadratic Programming (QCQP) problem. By introducing an auxiliary variable i, the problem can be equivalently reformulated as

$$\begin{aligned} \mathcal{P}7: \quad & \max_{\bar{\mathbf{v}}}\sum_{s=1}^{S}\bar{\mathbf{v}}^H\mathbf{R}_s\bar{\mathbf{v}} \\ & \text{s.t. } |\mathbf{v}_{\mathrm{a}}|^2=1,\ \mathrm{a}\ \in[1,\max\{M,N\}], \end{aligned} \tag{46}$$

where

$$\mathbf{R}_s=\begin{bmatrix}\mathbf{\Lambda}_s\mathbf{\Lambda}_s^H & 0\\ 0 & 0\end{bmatrix}, \quad \bar{\mathbf{v}}=\begin{bmatrix}\mathbf{v}\\ i\end{bmatrix}.$$

The problem remains non-convex due to the rank-one constraint. Noting that $\bar{\mathbf{v}}^H\mathbf{R}_s\bar{\mathbf{v}} = \text{tr}(\mathbf{R}_s\bar{\mathbf{v}}\bar{\mathbf{v}}^H)$, we define

the matrix $\mathbf{V} = \bar{\mathbf{v}}\bar{\mathbf{v}}^H$, which is positive semidefinite and constrained to have $\mathrm{rank}(\mathbf{V}) = 1$. By applying SDR method, we relax the rank-one constraint, thereby reformulating the problem as:

$$\mathcal{P}8: \quad \max_{\mathbf{V}} \sum_{s=1}^{S} \mathrm{tr}\left(\mathbf{R}_s \mathbf{V}\right) \\ \text{s.t.} \quad \mathbf{V}_{\mathrm{a,\,a}} = 1, \quad \mathrm{i} \in [1, \max\{\mathbf{M}, \mathbf{N}\} + 1], \ \mathbf{V} \succeq 0. \tag{47}$$

At this stage, problem $\mathcal{P}8$ can be transformed into a convex SDP problem, which can be efficiently solved using existing convex optimization techniques. In this work, the MOSEK solver is employed to numerically obtain the optimal solution to the SDP problem.

Since the optimal solution obtained via the SDR method is generally a positive semidefinite matrix, it is necessary to extract feasible solutions that satisfy the original problem's constraints in practical SIM phase shift optimization. To this end, the Gaussian randomization method is commonly employed to recover feasible solutions from the relaxed SDR solution. The core idea of Gaussian randomization involves performing eigenvalue decomposition on the SDR solution, followed by random sampling to approximate a rank-one solution that meets the problem constraints. Owing to its relatively low computational complexity and straightforward implementation, the Gaussian randomization method has been widely adopted in various wireless communication optimization problems. In this work, for problem $\mathcal{P}8$, the specific steps of the Gaussian randomization method are outlined as follows.

First, perform eigenvalue decomposition on the SDR solution matrix $\mathbf{V}$ to obtain the eigenvalue vector $\boldsymbol{\sigma}$ and the eigenvector matrix $\mathbf{P} \in \mathbb{C}^{\mathrm{a}\times\mathrm{a}}$. Next, generate a normalized complex Gaussian random vector $\mathbf{r} \in \mathbb{C}^{\mathrm{a}\times 1}$, which is then used to construct the candidate optimized phase shift vector as follows:

$$\mathbf{v} = \mathbf{P}\,\mathrm{diag}(\sqrt{\boldsymbol{\sigma}})\,\mathbf{r}. \tag{48}$$

This vector is then employed to construct the transmission coefficient matrix $\boldsymbol{\Omega} = \mathrm{diag}(\mathbf{v})$ which is subsequently substituted into the expression for the transmission rate in the HMIMO channel as follows:

$$\mathrm{v_{data}} = \log_2 \det\left(\mathbf{I} + \frac{\mathbf{HZH}^{\mathrm{H}}}{\mathrm{N_0\ B}}\right). \tag{49}$$

VII. Performance Evaluation

In this section, we validate the effectiveness of the SDR method under various parameter settings, demonstrating its capability to enhance the transmission rate. Furthermore, we analyze the influence of key system parameters on both the regret and transmission rate, and investigate the effects of delay and average packet size on the probabilistic delay bound. Unless otherwise specified, the key parameter settings are summarized in Table I. Additionally, we compare the performance of the proposed BCD algorithm with that of the low-complexity alternating optimization algorithm in terms of transmission rate.

Firstly, we illustrate the impact of the number of data streams on the transmission rate, propagation delay, and regret.

TABLE I: Simulation Parameters

Description	Value
Number of SIM Metasurface layers	3
Number of Meta-Atoms	36
Frequency f	7 GHz
Thickness of TX-SIM and RX-SIM	0.1 m
Wavelength λ	21.4 mm
Reference Path Loss PL_0	80 dB
Area of Meta-Atom	0.01 m^2
Rician Factor κ	20
Expected Waiting Time t_b	0.5 s
Mean of Packet Size l_d	100 Mb
Bandwidth B	10 MHz
Noise Power Spectral Density	-210 dBW/Hz
Transmission Power P	0.01 W
Expected Propagation Delay t_d	0.6 s

The results are presented in Fig. 3 through Fig. 4b. It can be observed that, as the number of data streams increases, the transmission rate improves, the propagation delay decreases, and the regret exhibits a downward trend.

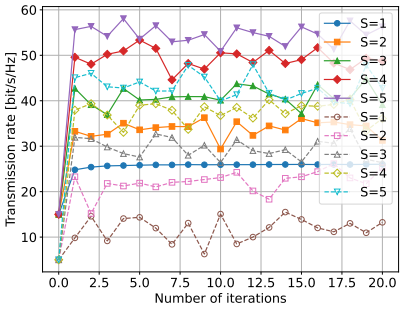

Fig. 3: *The relationship between the number of iterations and the data transmission rate v_{data} under varying numbers of data streams. The solid curves represent the performance of the proposed BCD algorithm, whereas the dashed curves correspond to the results obtained using the low-complexity AO algorithm.*

As illustrated in Fig. 3, although the transmission rate v_{data} in the HMIMO channel exhibits fluctuations across iterations, it generally follows an upward trend and eventually converges. This observation confirms the effectiveness of the SDR-based optimization approach. In comparison, the low-complexity AO algorithm achieves reduced computational overhead but demonstrates relatively lower optimization performance. Nevertheless, regardless of the algorithm used, the transmission rate increases with the number of data streams. This behavior is primarily attributed to the improved spatial reuse efficiency enabled by a greater number of data streams, thereby enhancing the overall system throughput. Among the tested configurations, the transmission rate attains its maximum when $S = 5$.

Fig. 4a illustrates the variation in propagation delay, with the initial value set to 0.6s. Overall, the propagation delay exhibits a decreasing trend as the number of iterations increases, demonstrating the effectiveness of the proposed BCD algorithm in optimizing delay. It is worth noting that when $S = 2$, the propagation delay is slightly higher than that of $S = 1$ (approximately 0.01s difference), suggesting that when the transmission rate is relatively low, increasing v_{data} has a limited impact on the regret $f(v_{\mathrm{data}}, t_d)$, leading to similar

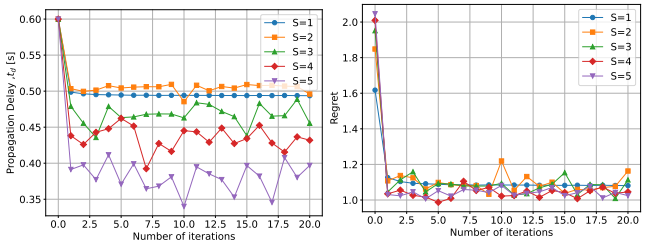

(a) *Propagation delay* t_d. **(b)** *Regret* $f(v_{data}, t_d)$.

Fig. 4: *Relationship between the number of iterations and propagation delay* t_d*/regret* $f(v_{data}, t_d)$ *under different numbers of data streams.*

optimization results for t_d. In contrast, when $S = 5$, the propagation delay is reduced by approximately 0.1s compared to the case of $S = 1$. This reduction is particularly significant in low-altitude intelligent network scenarios, where low transmission latency is essential to ensure real-time system performance. These results highlight that a slightly increase in the number of data streams can effectively reduce propagation delay and enhance system responsiveness.

Fig. 4b illustrates the trend of regret as iterations increase. For all values of the number of data streams, the regret consistently decreases with iteration count, though some fluctuations are observed during the convergence process. Notably, for $S = 4$ and $S = 5$, the regret exhibits the most rapid decline, and their final values are nearly indistinguishable. This behavior may be attributed to the structural constraint imposed by the limited number of metasurface layers, as well as the phenomenon of diminishing returns, wherein the incremental performance gain from adding additional data streams becomes marginal beyond a certain threshold. Nevertheless, under identical packet size l_d, the configuration with $S = 5$ achieves a lower propagation delay and higher transmission rate compared to other settings. Therefore, $S = 5$ represents a more advantageous configuration for practical deployment in low-altitude intelligent network scenarios.

In Fig. 5 and Fig. 6, we examine the impact of the number of meta-atoms per metasurface layer on the transmission rate and regret, with experimental parameters set as $L = K = 3$. The transmission rate shown is averaged over all iterations. Fig. 5 shows that the average transmission rate increases as the number of meta-atoms per SIM metasurface layer increases under both BCD algorithm and the low-complexity AO algorithm. Under identical meta-atom settings, the proposed method achieves a 51.47% average improvement in transmission rate over the low-complexity AO algorithm. In addition, for the same number of meta-atoms, using more data streams leads to a higher average transmission rate, which supports the trend observed in Fig. 3. However, it is important to note that when $M = N = 9$, the average transmission rate becomes nearly the same for $S \geq 2$. This is because a small number of meta-atoms leads to strong interference, and too many data streams reduce the efficiency of spatial reuse. Therefore, setting the number of meta-atoms to 9 in real-world SIM designs is not recommended, as it may lower system performance.

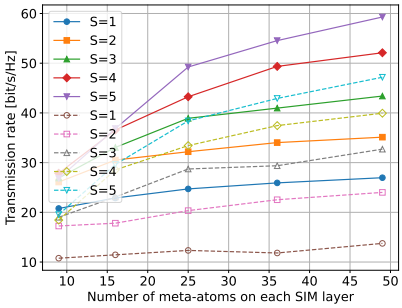

Fig. 5: *Relationship between the number of meta-atoms per metasurface layer and* v_{data} *under different numbers of data streams. Solid lines represent the results obtained using the BCD algorithm, while dashed lines indicate the performance of the proposed low-complexity AO algorithm.*

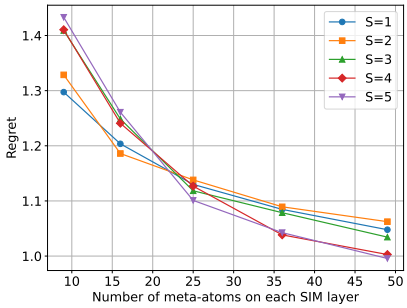

Fig. 6: *Relationship between regret and the number of meta-atoms per metasurface layer under different numbers of data streams.*

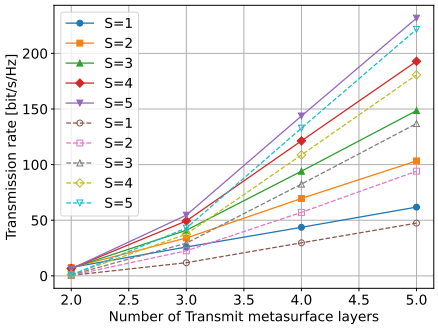

Fig. 7: *Relationship between the number of metasurface layers and the transmission rate* v_{data} *under different numbers of data streams. Solid lines present the results obtained using the BCD algorithm, while dashed lines show the performance of the low-complexity AO algorithm.*

Fig. 6 shows that as the number of meta-atoms increases, regret gradually decreases. However, it is important to note that when $M = N < 25$, the regret is lower for $S < 3$ than for $S \geq 3$, whereas when $M = N \geq 25$, higher regret performance is observed for $S \geq 4$. This suggests that when the number of meta-atoms on each metasurface layer is small, increasing the number of data streams does not significantly enhance system performance. The primary reason is that a small number of meta-atoms limits the system's degrees of freedom, resulting in reduced beamforming capability and

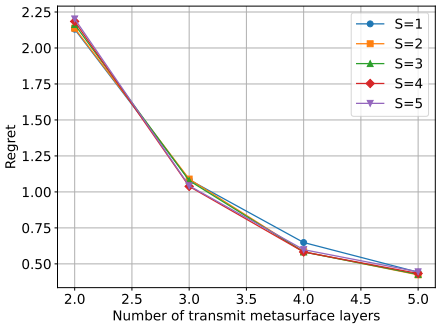

Fig. 8: *Relationship between the number of metasurface layers and transmission rate v_{data} under different numbers of data streams.*

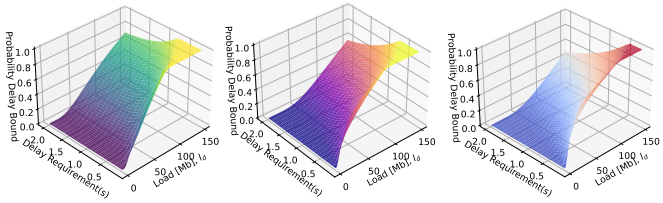

(a) $S = 1$ **(b)** $S = 3$ **(c)** $S = 5$

Fig. 9: *3D illustration of the probabilistic delay bound with respect to the delay requirement and system load.*

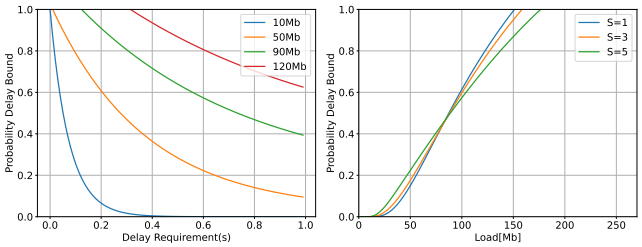

(a) *Total delay (T).* **(b)** *Load (l_d).*

Fig. 10: *Relationship between total delay (T)/load (l_d) and probabilistic delay bound under different load.*

less efficient interference management. In this case, fewer data streams lead to lower interference, and the optimization algorithm has limited flexibility, slowing the convergence of regret. In contrast, when the number of meta-atoms is large, the system gains more spatial degrees of freedom, enabling more effective interference mitigation and higher transmission rates. Additionally, the increased flexibility allows the SDR-based optimization to perform better, which accelerates the convergence of regret.

Furthermore, Fig. 7 illustrates that, regardless of whether the SDR method or the low-complexity AO algorithm is employed for optimization, the average transmission rate of the system significantly increases as the number of metasurface layers grows. Notably, this growth rate is substantially higher than that achieved by increasing the number of meta-atoms per metasurface layer. This is primarily because adding more metasurface layers introduces a greater diversity of scattering paths within the channel, thereby enhancing spatial reuse capabilities and effectively boosting the average transmission rate. Consequently, under the same conditions, the highest transmission rate is achieved when $S = 5$, and the SDR-based approach consistently outperforms the low-complexity AO algorithm in terms of performance. However, it is important to note that, given the limited total thickness of the SIM, excessively increasing the number of metasurface layers may lead to greater energy attenuation and increased structural complexity, thereby constraining the potential for further performance improvement.

Fig. 8 shows that as the number of metasurface layers increases, the average transmission rate improves while the regret gradually decreases, further confirming the performance enhancement brought by multi-layer structures. However, it is observed that when $L = K = 2$, the regret values across different data stream configurations remain close. As the number of metasurface layers increases to $L = K = 3$ or 4, the differences in regret become more pronounced across varying data stream quantities, indicating that higher spatial reuse capability leads to improved optimization performance. Nevertheless, when the number of layers increases further to $L = K = 5$, the regret values for different numbers of data streams converge, suggesting that the system is reaching its optimal structural configuration. At this point, the benefits of adding more data streams for regret reduction begin to saturate.

Fig. 10 provides a comprehensive three-dimensional illustration of the relationship among the probabilistic delay bound, the propagation delay, and the packet size. The parameters are set as follows: under fixed average transmission rates, the average transmission rate is 25.92 bps/Hz for $S = 1$, 40.96 bps/Hz for $S = 3$, and 54.55 bps/Hz for $S = 5$.

From the subplots in Fig. 10, it can be observed that as the packet size increases, the probabilistic delay bound also increases. This is because larger packets require longer transmission times within the network, which raises the probabilistic delay bound. Additionally, at lower total end-to-end delay T, the probabilistic delay bound is higher, since a stricter delay requirement increases the probability of exceeding that threshold. Moreover, when $S = 5$, the average transmission rate is the highest, resulting in the best performance in terms of both the probabilistic delay bound and propagation delay. This indicates that a higher number of data streams can improve spatial reuse efficiency, thereby reducing end-to-end propagation delay and optimizing the probabilistic delay bound. Conversely, when $S = 1$, the average transmission rate is the lowest, leading to the poorest performance in terms of the probabilistic delay bound and propagation delay. These results further demonstrate that appropriately increasing the number of data streams can effectively improve the system's delay performance, enhancing communication reliability and Quality of Service (QoS) assurance.

Fig. 10a illustrates the impact of total delay on the probabilistic delay bound, where the transmission rate is fixed and averaged at 40.86 bps/Hz. As shown in Fig. 10a, the probabilistic delay bound $P\{D > T\}$ decreases as the delay threshold T increases. This indicates that the likelihood of packets exceeding the delay threshold diminishes with a larger allowable delay. Moreover, a larger average packet size l_d

leads to a higher probabilistic delay bound, meaning the probability of delay violation increases. Conversely, for a fixed probabilistic delay bound, larger packets require a longer propagation delay. This implies that smaller packet sizes contribute to better delay performance in the HMIMO communication system. The main reason is that smaller packets allow the HMIMO channel transmission rate v_{data} to adequately handle incoming traffic, thus reducing propagation delay t_d. Consequently, the overall packet delay is mainly influenced by the transmission time within the HMIMO channel rather than by congestion or queuing delays. These results emphasize that appropriately managing packet size l_d is crucial for optimizing propagation delay t_d and improving the delay performance of the communication system.

Fig. 10b illustrates the relationship between the probabilistic delay bound $P\{D > 0.7\}$ and the average packet size l_d, under a fixed average transmission rate. The average transmission rates are set as follows: 25.92 bps/Hz for $S = 1$, 40.96 bps/Hz for $S = 3$, and 54.55 bps/Hz for $S = 5$. As observed in Fig. 10b, the probabilistic delay bound increases with the mean packet size l_d. This is because larger packets require longer transmission times, resulting in a higher probability of exceeding the delay threshold. In particular, when the packet size is less than 85 Mb, the probabilistic delay bound for $S = 1$ is lower than those for $S = 3$ and $S = 5$, indicating that $S = 1$ achieves the best performance in this range. This occurs because, for small packet transmission, the available channel resources with $S = 1$ are sufficient to support the data flow. However, when the packet size exceeds 85 Mb, the probabilistic delay bound for $S = 5$ becomes significantly better than those for other stream numbers, demonstrating the advantage of a larger number of data streams in transmitting large packets. Specifically, the average packet size at which the probabilistic delay bound reaches 1 (i.e., when T exceeds 0.7 s) is 150 Mb for $S = 1$, 158 Mb for $S = 3$, and 175 Mb for $S = 5$. This indicates that for larger data transmissions, increasing the number of data streams can effectively reduce the end-to-end propagation delay, thereby improving delay performance.

VIII. Conclusion

This paper proposes a SIM-assisted HMIMO aerial communication system designed to meet the stringent latency and reliability requirements of dynamic AAM scenarios. By integrating the TX-SIM and RX-SIM on eVTOL platforms, the system leverages precoding and combining techniques at both the transmitter and receiver ends to enhance performance. To address the trade-off between propagation delay and the probabilistic delay bound, we formulate a non-convex optimization problem, which is efficiently solved using a BCD framework combined with the SDR method. Further analysis reveals the impact of the number of data streams, meta-atom density, and the number of metasurface layers on delay performance and system regret. Additionally, we investigate the effects of system load and total delay T on the probabilistic delay bound. This work provides practical insights for deploying SIM-assisted HMIMO systems and lays the foundation for future research on scalable multi-eVTOL coordination and learning-based optimization under imperfect CSI.

Appendix

A. Proof of Theorem 1

Based on SNC, the queuing delay is defined as follows:

$$D_1 = \inf\{\tau \geq 0 : A(t) \leq A^*(t+\tau)\}. \tag{50}$$

Consequently, the event $\{D_1 > t_b\}$ implies $\{A(t) > A^*(t + t_b)\}$, and it follows that: $\{D_1 > t_b\} \subseteq \{A(t) > A^*(t + t_b)\}$ According to the stochastic arrival curve $A \sim \langle f, \alpha\rangle$ and the stochastic service curve $S \sim \langle g, \beta\rangle$, the probabilistic upper bound of the queuing delay can be expressed as [22]: $P\{D_1 > t_b\}$ represents that the probabilistic delay bound of D_1, which is also called an upper bound of the complementary cumulative distribution function (CCDF) of the packets delay t_b. i.e. the probability that the data packets wait in the buffer for more than t_b.

$$\begin{aligned}
&P\{D_1 > t_b\} \leq P\{A(t) - A^*(t+t_b) > 0\} \\
&\leq P\left\{ \sup_{0\leq\tau\leq t} [A(\tau,t) - \alpha(t-\tau)] + A \otimes \beta_{\text{data}}(t+t_b) \right. \\
&\quad \left. -A^*(t+t_b) > \inf_{0\leq\tau\leq t+t_b} [\beta_{\text{data}}(t+t_b-\tau) - \alpha(t-\tau)] \right\} \\
&\leq f \otimes g \left(\inf_{0\leq\tau\leq t+t_b} [\beta_{\text{data}}(t+t_b-\tau) - \alpha(t-\tau)] \right) \\
&\leq f \otimes g \left(\beta_{\text{data}}(t_b) \right)
\end{aligned} \tag{51}$$

In the last line of (51), we apply a sufficient stability condition: for all $t \geq 0$, we have $\beta(t) \geq \alpha(t)$.

We hold the service curve $\beta_{\text{data}}(t)$ for D_1 as

$$\beta_{\text{data}}(t) = v_{\text{data}} B t, \tag{52}$$

where v_{data} is the transmission rate in the HMIMO channel,the calculation formula of v_{data} is given in the subsection V. B denotes the system bandwidth and $g(x) = 0$. Here, $f(x)$ and $g(x)$ are bounding functions. Using equations (51) and (52), the probabilistic delay bound of D_1 becomes

$$P\{D_1 > t_b\} \leq f(v_{\text{data}} B t_b) \triangleq \bar{D}_1(t_b). \tag{53}$$

References

[1] A. P. Cohen, S. A. Shaheen, and E. M. Farrar, "Urban air mobility: History, ecosystem, market potential, and challenges," *IEEE Transactions on Intelligent Transportation Systems*, vol. 22, no. 9, pp. 6074–6087, 2021.

[2] B. Kim and H. Kim, "6g for uam communications: Challenges and visions," in *2022 13th International Conference on Information and Communication Technology Convergence (ICTC)*, 2022, pp. 1526–1528.

[3] S. Mishra and P. Palanisamy, "Autonomous advanced aerial mobility—an end-to-end autonomy framework for uavs and beyond," *IEEE Access*, vol. 11, pp. 136 318–136 349, 2023.

[4] T. Pasha, S. H. M, S. K R, B. S. D, and J. R. Munavalli, "Evaluation of uav path planning approaches for urban air mobility," in *2025 International Conference on Intelligent and Innovative Technologies in Computing, Electrical and Electronics (IITCEE)*, 2025, pp. 1–6.

[5] R. W. Ghatas, R. H. Mogford, S. A. Verma, R. D. Wood, G. M. R. Torres, and A. H. Farrahi, "Development of candidate airspace procedures for urban air mobility in the dallas area," in *2024 AIAA DATC/IEEE 43rd Digital Avionics Systems Conference (DASC)*, 2024, pp. 1–7.

[6] H. Wei, B. Lou, Z. Zhang, B. Liang, F.-Y. Wang, and C. Lv, "Autonomous navigation for evtol: Review and future perspectives," *IEEE Transactions on Intelligent Vehicles*, vol. 9, no. 2, pp. 4145–4171, 2024.

[7] S. R. Yelisetty and A. Kuriakose, "Autonomous air traffic management scheduling system," in *2024 IEEE International Conference on Electronics, Computing and Communication Technologies (CONECCT)*, 2024, pp. 1–6.

[8] A. A. Zaid, B. E. Y. Belmekki, and M.-S. Alouini, "evtol communications and networking in uam: Requirements, key enablers, and challenges," *IEEE Communications Magazine*, vol. 61, no. 8, pp. 154–160, 2023.

[9] J. Bae, H. Lee, and H. Lee, "A study on communication technologies for urban air mobility," in *2022 13th International Conference on Information and Communication Technology Convergence (ICTC)*, 2022, pp. 2235–2240.

[10] S. Al-Rubaye, C. Conrad, and A. Tsourdos, "Communication network architecture with 6g capabilities for urban air mobility," in *2024 IEEE International Conference on Consumer Electronics (ICCE)*, 2024, pp. 1–6.

[11] A. Manzoor, M. Ozger, D. Schupke, and C. Cavdar, "Combined airspace and non-terrestrial 6g networks for advanced air mobility," in *2024 20th International Conference on the Design of Reliable Communication Networks (DRCN)*, 2024, pp. 47–53.

[12] R. Deng, Y. Zhang, H. Zhang, B. Di, H. Zhang, H. V. Poor, and L. Song, "Reconfigurable holographic surfaces for ultra-massive mimo in 6g: Practical design, optimization and implementation," *IEEE Journal on Selected Areas in Communications*, vol. 41, no. 8, pp. 2367–2379, 2023.

[13] H. Wu, Y. Chen, Y. Ming, and Z. Wang, "Two-timescale beamforming optimization for downlink multi-user holographic mimo surfaces," *IEEE Transactions on Vehicular Technology*, vol. 73, no. 3, pp. 4476–4481, 2024.

[14] T. Gong, P. Gavriilidis, R. Ji, C. Huang, G. C. Alexandropoulos, L. Wei, Z. Zhang, M. Debbah, H. V. Poor, and C. Yuen, "Holographic mimo communications: Theoretical foundations, enabling technologies, and future directions," *IEEE Communications Surveys & Tutorials*, vol. 26, no. 1, pp. 196–257, 2024.

[15] R. Deng, B. Di, H. Zhang, H. V. Poor, and L. Song, "Holographic mimo for leo satellite communications aided by reconfigurable holographic surfaces," *IEEE Journal on Selected Areas in Communications*, vol. 40, no. 10, pp. 3071–3085, 2022.

[16] S. Hu, F. Rusek, and O. Edfors, "Beyond massive mimo: The potential of positioning with large intelligent surfaces," *IEEE Transactions on Signal Processing*, vol. 66, no. 7, pp. 1761–1774, 2018.

[17] C. Huang, A. Zappone, G. C. Alexandropoulos, M. Debbah, and C. Yuen, "Reconfigurable intelligent surfaces for energy efficiency in wireless communication," *IEEE Transactions on Wireless Communications*, vol. 18, no. 8, pp. 4157–4170, 2019.

[18] M. A. ElMossallamy, H. Zhang, L. Song, K. G. Seddik, Z. Han, and G. Y. Li, "Reconfigurable intelligent surfaces for wireless communications: Principles, challenges, and opportunities," *IEEE Transactions on Cognitive Communications and Networking*, vol. 6, no. 3, pp. 990–1002, 2020.

[19] J. An, C. Xu, D. W. K. Ng, G. C. Alexandropoulos, C. Huang, C. Yuen, and L. Hanzo, "Stacked intelligent metasurfaces for efficient holographic mimo communications in 6g," *IEEE Journal on Selected Areas in Communications*, vol. 41, no. 8, pp. 2380–2396, 2023.

[20] J. An, C. Yuen, C. Xu, H. Li, D. W. K. Ng, M. Di Renzo, M. Debbah, and L. Hanzo, "Stacked intelligent metasurface-aided mimo transceiver design," *IEEE Wireless Communications*, vol. 31, no. 4, pp. 123–131, 2024.

[21] Z. Wang, J. Zhang, and T. Huang, "Determining delay bounds for a chain of virtual network functions using network calculus," *IEEE Communications Letters*, vol. 25, no. 8, pp. 2550–2553, 2021.

[22] P. Li, Y. Wei, N. Li, T. Huang, and N. Jin, "Packet loss and delay analysis for a wireless fading channel using stochastic network calculus," in *2022 14th International Conference on Wireless Communications and Signal Processing (WCSP)*, 2022, pp. 1070–1074.

[23] G. Wang, M. Lai, F. Huang, and T. Li, "A stochastic network calculus for service performance in wireless mesh networks," in *2010 5th International Conference on Computer Science & Education*, 2010, pp. 1685–1688.

[24] W. Jiao, M. Sheng, K.-S. Lui, and Y. Shi, "End-to-end delay distribution analysis for stochastic admission control in multi-hop wireless networks," *IEEE Transactions on Wireless Communications*, vol. 13, no. 3, pp. 1308–1320, 2014.

[25] H.-T. Wai, W.-K. Ma, and A. M.-C. So, "Cheap semidefinite relaxation mimo detection using row-by-row block coordinate descent," in *2011 IEEE International Conference on Acoustics, Speech and Signal Processing (ICASSP)*, 2011, pp. 3256–3259.

[26] Q. Wu and R. Zhang, "Intelligent reflecting surface enhanced wireless network via joint active and passive beamforming," *IEEE Transactions on Wireless Communications*, vol. 18, no. 11, pp. 5394–5409, 2019.

[27] J. V. T. Ribeiro, M. C. R. Murça, and W. S. S. Souza, "Tradeoffs between safety and efficiency from dynamic airspace geofencing for advanced air mobility," in *2022 IEEE/AIAA 41st Digital Avionics Systems Conference (DASC)*, 2022, pp. 1–8.

[28] K.-Y. Tsai, G.-Y. Meng, T.-L. Wu, M.-H. Zheng, W.-Y. Wang, C.-M. Kung, Y.-C. Chen, C.-F. Huang, T.-C. Hsieh, H.-S. Hsu, H.-D. Lin, and J.-X. Shi, "evtol, uam, and aam: Brief development history and implementation outlook of the united states," in *2023 IEEE International Conference on e-Business Engineering (ICEBE)*, 2023, pp. 287–296.

[29] S. Shahriar Ahmed, G. Fountas, V. Lurkin, P. C. Anastasopoulos, Y. Zhang, M. Bierlaire, and F. Mannering, "The state of urban air mobility research: An assessment of challenges and opportunities," *IEEE Transactions on Intelligent Transportation Systems*, vol. 26, no. 2, pp. 1375–1394, 2025.

[30] H. Niu, X. Lei, J. An, L. Zhang, and C. Yuen, "On the efficient design of stacked intelligent metasurfaces for secure siso transmission," *IEEE Transactions on Information Forensics and Security*, vol. 20, pp. 60–70, 2025.

[31] J. An, M. Di Renzo, M. Debbah, and C. Yuen, "Stacked intelligent metasurfaces for multiuser beamforming in the wave domain," in *ICC 2023 - IEEE International Conference on Communications*, 2023, pp. 2834–2839.

[32] X. Yao, J. An, L. Gan, M. Di Renzo, and C. Yuen, "Channel estimation for stacked intelligent metasurface-assisted wireless networks," *IEEE Wireless Communications Letters*, vol. 13, no. 5, pp. 1349–1353, 2024.

[33] S. Lin, J. An, L. Gan, M. Debbah, and C. Yuen, "Stacked intelligent metasurface enabled leo satellite communications relying on statistical csi," *IEEE Wireless Communications Letters*, vol. 13, no. 5, pp. 1295–1299, 2024.

[34] K. Xiong, Z. Chen, J. Xie, S. Leng, and C. Yuen, "Digital twin-based sim communication and flight control for advanced air mobility," 2025. [Online]. Available: https://arxiv.org/abs/2501.01837

[35] J. An, C. Yuen, Y. L. Guan, M. Di Renzo, M. Debbah, H. V. Poor, and L. Hanzo, "Two-dimensional direction-of-arrival estimation using stacked intelligent metasurfaces," *IEEE Journal on Selected Areas in Communications*, 2024.

[36] K. Feng and F. Baccelli, "Spatial network calculus and performance guarantees in wireless networks," *IEEE Transactions on Wireless Communications*, vol. 23, no. 5, pp. 5033–5047, 2024.

[37] Y. Sun, B. Zhang, and R. Li, "Research on real-time of hybrid scheduling for mine industrial ethernet with network calculus," in *2010 8th World Congress on Intelligent Control and Automation*, 2010, pp. 1145–1149.

[38] K. Xiong, S. Leng, L. Chen, D. Zhang, C. Huang, and C. Yuen, "Ris-aided trajectory optimization in layered urban air mobility," *IEEE Internet of Things Journal*, vol. 12, no. 2, pp. 2188–2202, 2025.

[39] Z. Tao, W. Quan, and W. Gao-Cai, "Performance analysis on m2m communication network based on stochastic network calculus," in *2014 IEEE 13th International Conference on Trust, Security and Privacy in Computing and Communications*, 2014, pp. 865–870.

[40] Y. Jiang, "A note on applying stochastic network calculus," in *Proc. SIGCOMM*, vol. 10, no. 2010, 2010, pp. 16–20.

[41] A. Papazafeiropoulos, J. An, P. Kourtessis, T. Ratnarajah, and S. Chatzinotas, "Achievable rate optimization for stacked intelligent metasurface-assisted holographic mimo communications," *IEEE Transactions on Wireless Communications*, vol. 23, no. 10, pp. 13 173–13 186, 2024.

[42] X. Hu, R. Deng, B. Di, H. Zhang, and L. Song, "Holographic beamforming for ultra massive mimo with limited radiation amplitudes: How many quantized bits do we need?" *IEEE Communications Letters*, vol. 26, no. 6, pp. 1403–1407, 2022.

[43] O. T. Demir, E. Bjornson, and L. Sanguinetti, "Channel modeling and channel estimation for holographic massive mimo with planar arrays," *IEEE Wireless Communications Letters*, vol. 11, no. 5, pp. 997–1001, 2022.